The Backscatter Gating method for time, energy, and position resolution characterization of long form factor organic scintillators

Hunter N. Ratliff,[a,1] **Toni Kögler,**[b,c] **Guntram Pausch,**[d] **Lena M. Setterdahl,**[a] **Kyrre Skjerdal,**[a] **Joseph A. Turko,**[e] **and Ilker Meric**[a,1]

[a] *Western Norway University of Applied Sciences, Department of Computer science, Electrical engineering and Mathematical sciences, Bergen, Norway*

[b] *Helmholtz-Zentrum Dresden — Rossendorf, Institute of Radiooncology — OncoRay, Dresden, Germany*

[c] *OncoRay — National Center for Radiation Research in Oncology, Faculty of Medicine and University Hospital Carl Gustav Carus, Technische Universität Dresden, Helmholtz-Zentrum Dresden — Rossendorf, Dresden, Germany*

[d] *Target Systemelektronik GmbH & Co. KG, Wuppertal, Germany*

[e] *Institute of Radiation Physics, Helmholtz-Zentrum Dresden — Rossendorf, Dresden, Germany*

E-mail: Hunter.Ratliff@hvl.no, Ilker.Meric@hvl.no

Abstract: This work details a Compton-scattering-based methodology, referred to as Backscatter Gating (BSG), for characterizing the time, energy, and position resolutions of long form factor organic scintillators using a single, fairly minimal measurement setup. Such a method can ease the experimental burden in scenarios where many such scintillator elements may need to be individually characterized before assembly into a larger detector system. A thorough theoretical exploration of the systematic parameters is provided, and the BSG method is then demonstrated by a series of experimental measurements. This "complete" characterization via the BSG method is novel, having previously been used primarily for energy resolution characterization. The method also allows for determination of the assembled scintillator's technical attenuation length and provides a means of verifying the presence or absence of flaws within the scintillator or its optical coupling.

Keywords: Trigger concepts and systems (hardware and software); Detector alignment and calibration methods (lasers, sources, particle-beams)

[1]Corresponding author.

Contents

1 Introduction

Long form factor scintillation detectors (also known as high aspect ratio detectors) have a variety of applications. These detectors — often in the shapes of rectangular bars, cylindrical rods, or thin fibers — can provide insight on where interactions occur spatially, enabling their usage in camera-type detector setups. With two dimensions constrained by the relative "thinness" of the detector, the interaction position in the third dimension, along the scintillator's length, is typically determined by comparing signals from readout sensors placed on both ends of the scintillator. For a single interaction, this comparison can involve the difference of arrival times of the scintillation light, the relative amounts of light detected at each end, or some combination of both.

For the camera-type detection setups employing multiple long form factor detectors, scattering kinematics are used for determining the possible initial trajectories of incident radiation, which are then provided to image reconstruction algorithms. Imaging performance is dependent on the energy, coincident time, and position (or depth of interaction) resolutions of the scintillator [1], which themselves are dependent on a number of variables including detector dimensions, material, surface finish, reflective properties of the wrapping material, and more. Characterizing these resolutions is an important step in determining what scintillator materials, shapes, and preparations will perform most optimally for a given application. Traditionally, these resolutions are evaluated with different measurements.

To obtain the most precise position and timing resolutions in a characterization measurement, the depth-of-interaction (DOI) along the scintillator's length needs to be constrained to as small of a spatial region as possible, typically achieved with collimated radioactive sources or an annihilation photon coincidence detection with an ancillary detector and a β^{+} decay source, such as ^{22}Na [2]. One downside of such approaches is the long acquisition times necessary to obtain adequate measurement statistics.

Energy resolution measurements in organic scintillators are complicated by the fact that photon reactions are dominated by Compton scattering while photoabsorption is nearly negligible, making traditional photopeak identification approaches with simple gamma-ray-emitting radioactive sources nonviable. An ideal direct energy resolution measurement involves deposition of a known constant amount of energy in the scintillator, often achieved with an electron or ion beam [3], coincidence measurements with cosmic muons [4], or collimated Compton coincidence techniques [5, 6]. While these methods are effective, they often require a fair amount of resources (physical, financial, temporal), are complex, and can be of limited availability [7].

This work takes place in the context of the NOVO project (NeutrOn and gamma-ray imaging for real-time range VerificatiOn and image guidance in particle therapy) [1], wherein a detector array of organic scintillator bars is being constructed whose individual scintillator elements will require these resolution characterizations. The discussed resolution measurement approaches have been employed for characterizing the elements of similar modular neutron detector array setups [8, 9]; however, provided the numerous elements in the planned NOVO array, a simpler, more streamlined methodology would be of great benefit to the upcoming experimental campaigns involving the under-construction prototype detection system.

A methodology for using a Compton coincidence technique known as Backscatter Gating (BSG) [7, 10] alone to measure these resolutions — in a single setup — is outlined in this work. The method is explained in detail in the following section, but, in short, it allows for isolation of a spatially constrained and quasi-monoenergetic electron energy deposition within the scintillator of interest using only a gamma-ray-emitting radioactive source and a single ancillary detector.

A theoretical exploration of the impacts of the various experimental variables in a typical Backscatter Gating setup is presented to provide further insight on this method's limits and its theoretical best practices, and a set of experimental measurements follow demonstrating the method in use. The Backscatter Gating method's simplicity and minimal requirements, in terms of equipment and radioactive sources, make it an appealing alternative for characterization of long form factor scintillators, especially when needing to characterize a large number of individual elements composing a camera-type detector setup. While the BSG method is more broadly applicable than the context of the array being constructed in the NOVO project, the plastic scintillator bars used in this work have dimensions corresponding to those planned in early designs for the prototype detection system. However, they are of a different organic material from those planned for the under-construction array [11].

2 Theory and methods

Backscatter Gating (BSG) takes advantage of the physics and geometry of photon scattering to constrain both the energy deposited and interaction position of successfully "gated" coincident events. In general, a BSG setup consists of just three elements: a gamma-ray-emitting radioisotope source, the long form-factor scintillator being characterized, and an energy-calibrated, high atomic number (and ideally high energy resolution) detector, referred to as the BSG detector. By placing the source between the two detectors and only triggering on events where both fire, the vast majority of the coincident events are occurrences of the emitted photon undergoing Compton scattering in the long organic scintillator with a backwards angle and then undergoing photoelectric absorption in the BSG detector. The organic scintillator's low atomic number makes Compoton scattering the dominant reaction mechanism for most radionuclide-emitted gamma rays while the BSG detector's high atomic number makes photoelectric absorption the dominant reaction for both primary and especially the lower-energy, backscattered gamma rays. Then, by further gating on the narrow peak of events depositing in the BSG detector the known remaining photon energy following a 180° Compton scatter, events corresponding to a single recoil electron energy in the long scintillator are isolated. By positioning the radioisotope near the long scintillator and placing adequate distance between the two detectors, geometry (solid angle) and scattering kinematics also constrain the portion of the long scintillator's length in which these single-energy recoil electron events occur to a fairly small region. This is demonstrated shortly.

In this work, an EJ-200 [12] organic plastic scintillator bar of dimensions $10 \times 10 \times 200\ \mathrm{mm}^3$ is characterized. The sides of the bar are wrapped in a Teflon reflector layer followed by a black light-tight layer, and both ends are optically coupled to Hamamatsu R5611A PMTs [13]. A $\varnothing 25.4\ \mathrm{mm} \times 25.4\ \mathrm{mm}$ $CeBr_3$ scintillator coupled to a Hamamatsu R13478 PMT [14] is used for detection of the backscattered gamma rays and is placed perpendicularly to the scintillator bar. Radioisotope sources, encapsulated in small plastic disks[1] and held in a custom 3D-printed stand, are placed as close as possible to the bar on the side between the two detectors and in line with the $CeBr_3$ detector. ^{137}Cs was the primary source used in this work, but measurements with ^{60}Co, ^{57}Co, and ^{54}Mn were also made to sample other recoil electron energies. This setup is shown in Figure 1. The gap between the two detectors was kept at a fixed distance of 80 mm, unless stated otherwise.

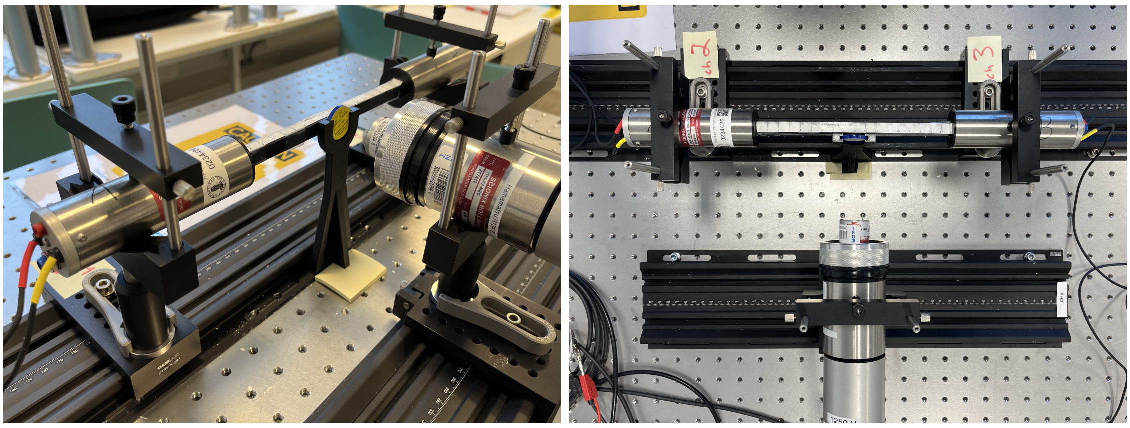

Figure 1: Arrangement of detectors used for BSG measurements from an angle (left) and straight above (right).

The output analog signals are digitized with a CAEN DT5730S digitizer [15] and acquired with the CAEN CoMPASS software [16]. The signals from the bar PMTs undergo constant fraction discrimination with 75 % CFD fraction, selected to minimize variance of the coincident time resolution as a function of source position along the scintillator bar's length, and 6 ns CFD delay. Coincidence logic was set to require detected events in the $CeBr_3$ and at least one of the two bar PMTs. Default settings were otherwise employed. The list-mode output from CoMPASS is further analyzed with custom Python scripts written for this work to assemble the true triple coincident events, requiring the $CeBr_3$ detector and both ends of the bar all firing in the default

[1]Exempt quantity radioactive disk sources, manufactured by Spectrum Techniques, LLC.

96 ns coincidence window[2] used for double coincidences in CoMPASS, and then a gate is applied on those events whose energy deposited in the $CeBr_3$ fall within the backscatter peak energy window, taken in this work to be $\pm 2\sigma$ of the 180° scattered photon energy peak in the $CeBr_3$ detector.

In this setup the source and BSG detector's center are kept along a line perpendicular to the long scintillator, $\perp_{src}$, at position p relative to the center of the long scintillator's length; when shifting the source laterally, the BSG detector is shifted along with it. Figure 2 depicts a schematic of the experimental setup with the key variables labeled: Compton scattering angle θ, distance between source and long scintillator x, distance between BSG detector and long scintillator d, distance ℓ along the long scintillator of first interaction from the perpendicular $\perp_{src}$ intersecting the source and BSG detector, first interaction's depth along the bar's width w, second interaction's depth from the BSG detector's face z, and second interaction's radial distance r from $\perp_{src}$.

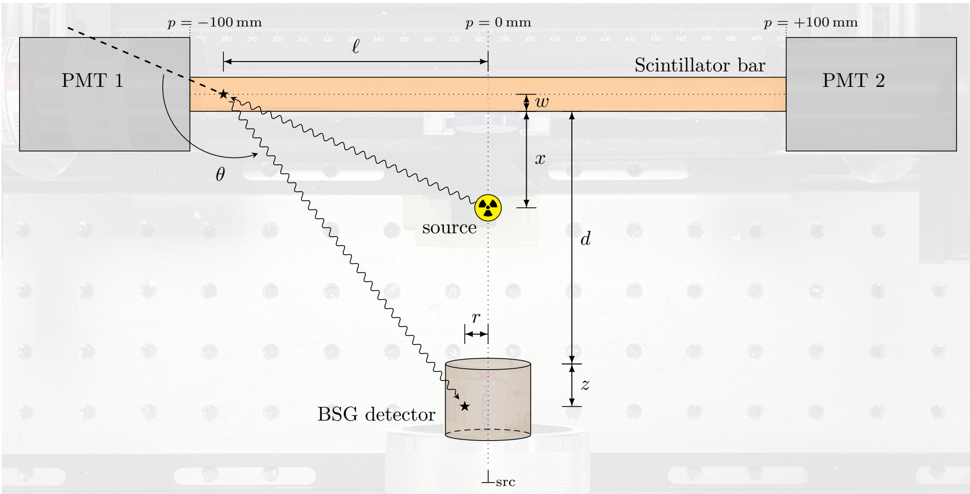

Figure 2: Illustration of relevant dimensions in a BSG measurement.

The variables which can be controlled are the distances between the two detectors d and the position of the source between them x; these will have a substantial impact on how localized the backscatter-gated recoil electrons are along the bar's length and the range of electron energies which will ultimately be able to satisfy the coincident criteria and be detected. The two extremes for source positioning are affixing the source to either detector. Figure 3 illustrates the impact of this decision, along with distance between the two detectors, on what BSG recoil electrons will be detected in terms of their energies, locations, and intensities as a function of both d and the extremes of x. The derivation of these relationships is detailed in Appendix A. Note that since ℓ is relative to the source perpendicular's $\perp_{src}$ absolute position p (where $p = 0$ is the center of the scintillator bar), the only bearing p would have on these calculations is the maximum possible value of ℓ.

This illustrates that placing the two detectors too close to each other causes the range of recoil electron energies associated with each position along the bar (and, to a lesser extent, the range of

[2]A much shorter coincidence window, ± 8 ns, was employed for comparing the two bar PMT signals. However, both were required to fall within 96 ns of the $CeBr_3$ BSG detector signal. While CoMPASS's default 96 ns coincidence window was sufficient for the low-activity sources used in this work, a shorter, more optimized coincidence window would be necessary if using a high-activity source to avoid triggering on unwanted coincidences from interactions of two separate decay emissions (and would have the added benefit of increasing the maximum possible coincident event rate).

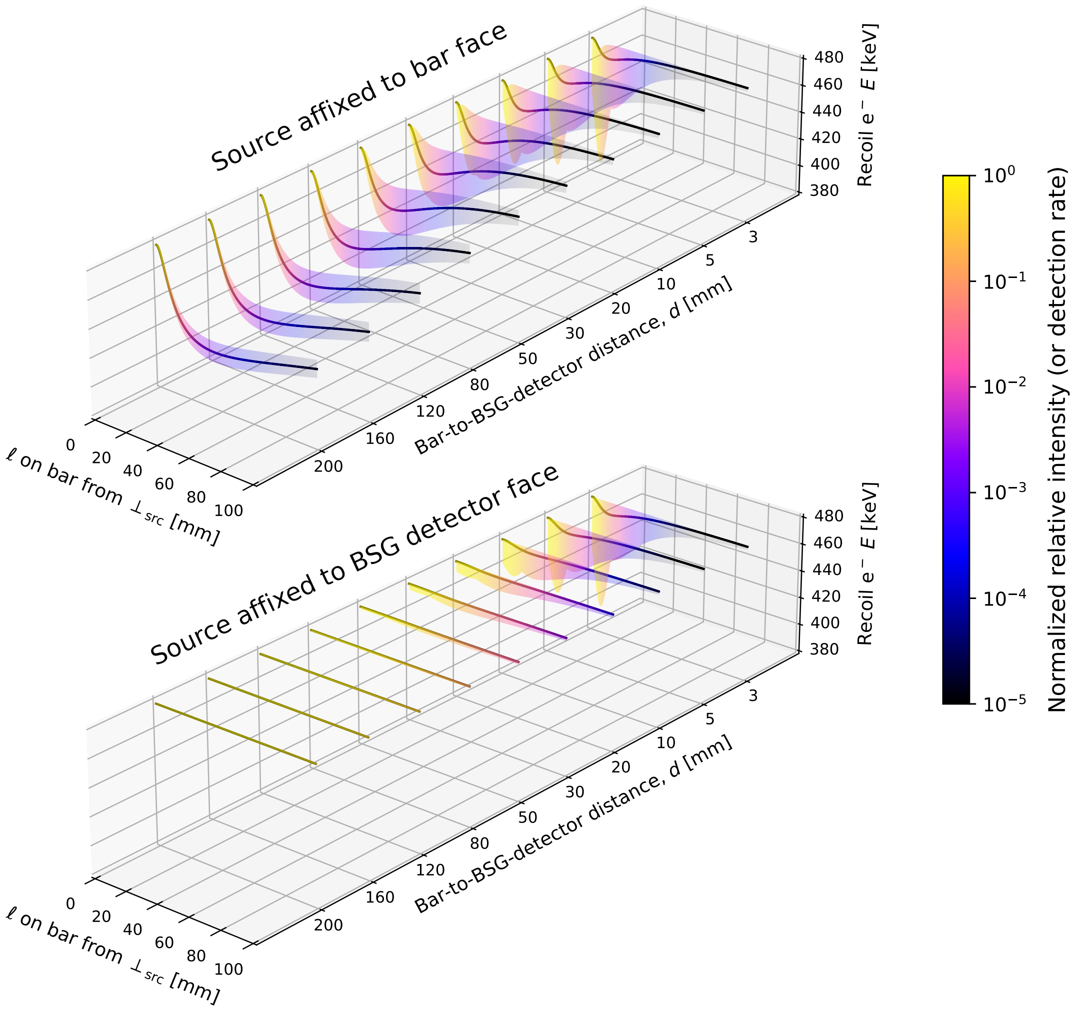

Figure 3: Shown for the 661.66 keV gamma-ray emission of ^{137}Cs scattering in the long scintillator bar and then being absorbed in the BSG detector are the nominal recoil electron energies in the bar, their ranges of possible energies, and their normalized relative intensities (or what can be thought of as normalized detection rates) as a function of the distance d between the scintillator bar and BSG detector and the first interaction's distance ℓ from the perpendicular $\perp_{\rm src}$ from the bar intersecting the source and BSG detector, for the source affixed to either the bar (top) or the BSG detector (bottom), using the physical detector dimensions of this work and assuming interactions nominally occur along a detector's centerline. The ranges of electron energies in the bands are determined by accounting for interactions being able to happen anywhere within the volume of the BSG detector. The relative intensity for each interaction position is a scaling factor accounting for the probability an emission will be bound for that position on the bar from the source, the solid angles involved in the two interactions, and the Klein-Nishina differential scattering cross section for the position's corresponding scattering angle, and it is normalized for each distance linearly to unity at the highest intensity, where the interaction position is in line with the source and BSG detector, $\ell = 0$ mm.

positions along the bar with high event rates) to grow, which is undesirable. While a BSG detector with high energy resolution would still be capable of gating on a narrow range of scattered photon energies with confidence, this is not ideal for a detector producing broader photopeaks and would ultimately result in contamination of the recoil electron energy distribution with those lower-energy electrons from <180° scatters.

More notably, the positioning of the source allows for two different "modes" of BSG operation. With the source affixed to the long scintillator bar and at still relatively small detector-to-detector distances (on the order of a few cm), most of the detected coincident events correspond to maximum-energy recoil electrons in a very small range of positions along the long scintillator's length; moving the two detectors further apart only amplifies this effect. When the source is affixed to the BSG detector, increasing distance between the two detectors dramatically decreases the range of electron energies detected to only those very close to the 180° scattering and more evenly distributes where these Compton interactions occur along the length of the bar.

As a means of verifying this theory-based deterministic calculation methodology, simulations of the two arrangements with detector-to-detector distances of 20 mm, 80 mm, and 150 mm were conducted with the PHITS 3.33 [17] general purpose Monte Carlo particle transport code. Figure 4 shows the recoil electron energy distributions within the bar, with each distribution's peak normalized to unity, and illustrates the spreading of detected electron energies at various detector distances and how much more constrained the range of electron energies is when the source is affixed to the BSG detector. Note that this spread of energies will have an impact on the observed energy resolutions of the detectors, discussed in more detail later.

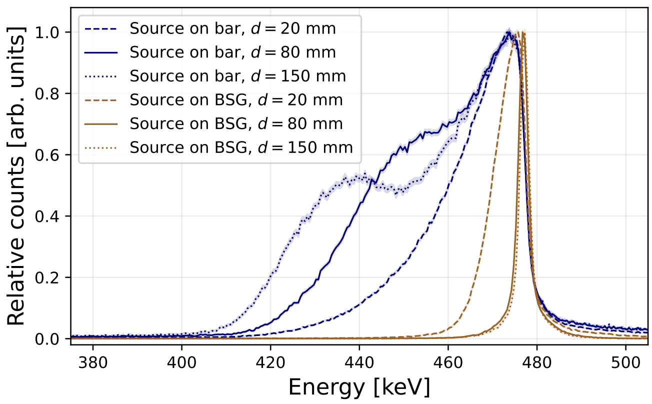

Figure 4: PHITS-simulated energy deposition spectra in the scintillator bar for ^{137}Cs emissions backscattering in the bar and interacting in the BSG detector, for various source placements and detector-to-detector distances d. For comparison of relative widths, the spectra have been scaled to have maxima of unity. The lines' error bands denote the simulations' statistical uncertainties.

However, while this spread in energies may seem quite severe for the "Source on bar" arrangement, the electron energies closest to the true backscatter recoil energy are in fact quite spatially isolated in the bar, as shown in Figure 5 and predicted earlier in the calculations shown in Figure 3, where the correlation between electron energy deposited and position along the bar is also clearly visible and most amplified at higher detector-to-detector distances. Though the Monte Carlo simulations more comprehensively account for all physics involved, they also require numerous orders of magnitude more time to simulate with sufficient statistics relative to the deterministic calculations (hours versus seconds); trustworthy theoretical calculations allow much more rapid comparison of various BSG experiment setups.

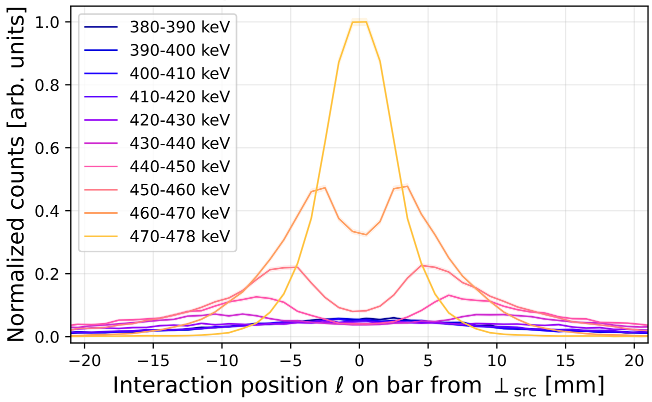

Figure 5: PHITS-simulated spatial distributions of various recoil electron energies in the scintillator bar for emissions from a ^{137}Cs source, affixed to the bar, backscattering in the bar and then going on to interact in the BSG detector, with $p = 0$ mm and $d = 80$ mm. The lines' error bands denote the simulations' statistical uncertainties.

In this work, since interaction position resolution is to be characterized, the first arrangement with the source affixed close to the long scintillator bar was selected. In cases where solely fine characterization of the scintillator's energy resolution is desired, with no consideration of depth of interaction, the other arrangement with the source affixed to the BSG detector is more suitable; note that this arrangement also comes at the expense of measurement statistics due to the longer flight path required, and thus smaller solid angle, of the photons to make the trip from the radioisotope source to the long scintillator and then back to the BSG detector onto which the source is attached.

At a set position (source centered on bar $p = 0$ mm, detector-to-detector distance $d = 80$ mm), BSG measurements were made with four different radioactive sources — ^{137}Cs, ^{60}Co, ^{57}Co, and ^{54}Mn — to provide an estimate of the energy, coincident time, and position resolutions as a function of light output of the long scintillator bar. The nominal detector-to-detector distance of 80 mm was selected to achieve a balance between spatially isolating the maximum-energy recoil electrons while not overly decreasing the solid angle of the required interactions (increasing measurement time required to collect adequate statistics). A further sixteen measurements were made with only ^{137}Cs. Eight were made at the same $p = 0$ mm but with the detector-to-detector distance varied ($d = 5,\ 10,\ 20,\ 30,\ 50,\ 80,\ 150$, and 300 mm)[3] to evaluate any potential effects on the energy and time resolutions. Eight were made at the same $d = 80$ mm but with the source and BSG detector shifted laterally, in steps of 20 mm along the bar's whole length ($p = \pm 20,\ \pm 40,\ \pm 60$, and ± 76 mm)[3], to quantify the ability of determining interaction position, attenuation length, and whether time or energy resolutions notably varied with position (which serves as a test of material homogeneity of the scintillator bar along its length and quality of the optical coupling on both ends of the bar).

[3]These experimental detector-to-detector distances and source positions are accurate to ±1 mm.

3 Results and discussion

After offline building of all triple-coincident events — where all three PMTs fired — the event-wise energy deposition/light production in the two scintillators is plotted against each other for a ^{137}Cs source affixed to the center of the long scintillator ($p = 0$ mm) with the BSG detector 80 mm away, shown in Figure 6. A clear peak is visible corresponding to backscattered events. Using Compton kinematics, the 661.66 keV emitted gamma ray, after a 180° scatter, remains with 184.32 keV (which is then fully absorbed by the BSG detector) with the difference of 477.34 keV imparted onto the recoil electron (which is typically stopped entirely within the long scintillator bar[4]).

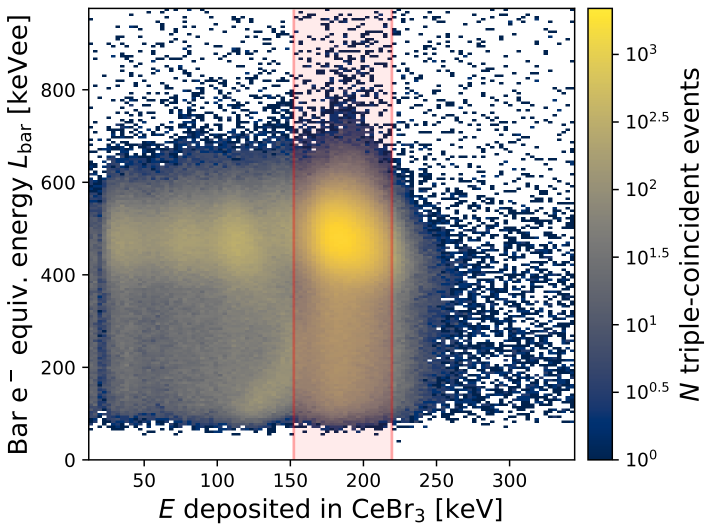

Figure 6: Energy depositions from a ^{137}Cs source in the BSG detector and scintillator bar for only triple-coincident events, with $p = 0$ mm and $d = 80$ mm and the BSG peak $\pm 2\sigma$ highlighted in red.

This 184 keV photopeak is clearly dominant in the energy spectrum of the $CeBr_3$ BSG detector, shown in Figure 7. This photopeak is fit with a Gaussian distribution, and a gate consisting of the mean plus or minus two standard deviations is set, illustrated as the vertical red band here and earlier in Figure 6. Events lying within this band are referred to those as lying in the backscatter peak; all further analysis in this work only considers events lying within the backscatter peaks. This $\pm 2\sigma$ gate width was selected for maximizing statistics while keeping the gated electrons spatially tightly constrained. A narrower gate would slightly improve this constraint but at the expense of statistics.

As noted earlier, the recoil photons striking the BSG detector are not truly monoenergetic. Thus, attempting to calculate the $CeBr_3$ BSG detector's energy resolution $\Delta E/E$ "at 184 keV" from the fit parameters, mean μ and full width at half maximum (FWHM), of Figure 7 with Equation 3.1 would yield a value slightly above 20 %, much higher than expected for this scintillator.

$$\Delta E/E = 100\% \times \mathrm{FWHM}_L/\mu_L \tag{3.1}$$

[4]A 477 keV electron has, from the NIST ESTAR database [18], a CSDA (continuous slowing down approximation) range of about 1.6 mm in "plastic scintillator" material.

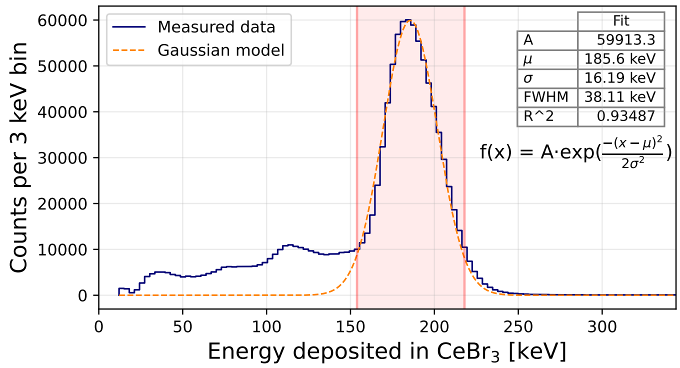

Figure 7: Energy deposition spectrum in the $CeBr_3$ BSG detector for only triple-coincident events, using a ^{137}Cs source with the backscattered photon peak used for gating highlighted in red.

The energy resolutions of the photopeak measurements used to energy calibrate the $CeBr_3$ BSG detector, where incident photons from each source were truly monoenergetic, lead one to expect an energy resolution at 184 keV of around 12 %. Estimating the variance of the measured peak $\sigma^2 = (16.2\,\text{keV})^2$ as the sum of the variance attributable to the expected 12 % energy resolution $(9.6\,\text{keV})^2$ and the variance from the spread of backscattered photon energies σ^2_{spread} attributable to the source and detector geometry, one finds $\sigma^2_{\text{spread}} = (13.1\,\text{keV})^2$. This spread is comparable to the energy spread found in the earlier PHITS simulations of the experimental setup (which do not include energy resolution effects[5]), and it is important to note that this energy spread is identical for both the BSG detector and the scintillator bar since it is determined by geometry and is independent of detector material.

Projecting the events within this $\pm 2\sigma$ band onto the vertical axis of Figure 6 yields Figure 8. Note that when first performing these analyses that the "electron-equivalent energy" axes of Figures 6 and 8 are instead just the measured integrated signal charge of the two PMTs summed (in arbitrary ADC channel units); for easier interpretation here they have been converted to light output (electron equivalent energy) units with the calibration curve shown in Figure 9, discussed shortly.

Here, a normally-distributed peak, with a lower-energy tail from electrons created near the bar's edge escaping[6] and random coincidences, indicative of the 477 keV recoil electron is visible. It can be fit with a Gaussian function, and from that the energy resolution can be calculated with Equation 3.1 with the fit's mean and FWHM.

Over the sixteen ^{137}Cs measurements described earlier, energy resolution of this EJ-200 bar was on average (27.3 ± 1.3) % with no statistically significant trend as a function of d nor p. If a very narrow backscatter peak gate of width 8 keV, centered at 184 keV, is set instead of the $\pm 2\sigma$ gate, this

[5]As further confirmation, in the BSG experiment simulations an additional PHITS [T-Deposit] tally was made including energy resolution model parameters derived from a fit of the experimentally obtained energy resolutions of the $CeBr_3$ detector (from the energy calibration photopeaks) that only counted photons that had already scattered in the scintillator bar; this yielded a simulated $\Delta E/E$ of 21.4 %, quite close to that observed experimentally in Figure 7.

[6]Simulations with PHITS confirm that the magnitude of the lower-energy tail relative to the peak is strongly correlated with the inverse of the bar's cross-sectional size. This is expected as the 477 keV electron has a range of ~1.6 mm (see [4]), which is of similar order to the thin dimensions of the bar. In addition, with a higher-activity source or the two detectors being placed close together, random coincidences would also contribute more significantly to this lower-energy tail.

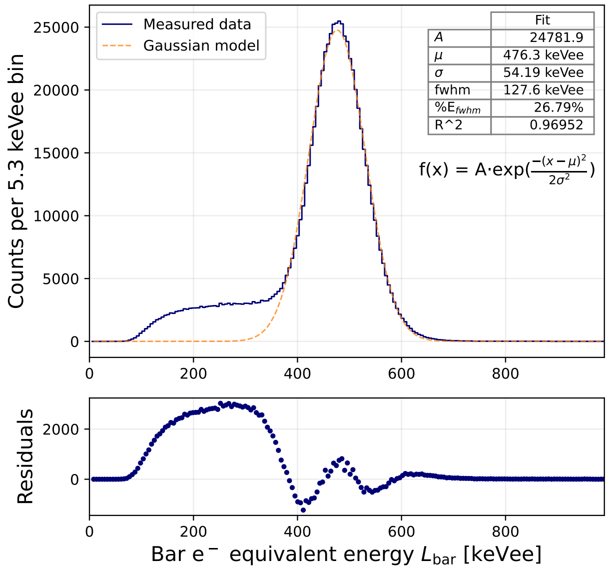

Figure 8: Energy deposition spectrum, obtained from the summed signal of both bar PMTs, in the long scintillator bar for events falling within the BSG peak highlighted in Figure 6.

energy resolution is slightly improved by 2 % to (25.3 ± 1.3) %. This is notably higher than other literature values for the energy resolution of EJ-200 in similar form factors and preparations [2, 11]. The known spread of recoil electron energies contained in the BSG peak, $\sigma^2_{\text{spread}} = (13.1\,\text{keV})^2$, discussed earlier in the context of the BSG detector, contributes a small part to this (correcting for the spread reduces $\Delta E/E$ by nearly 1 %), and this poorer performance is believed to be at least partially attributable to "ringing" present in the signals of the bar's PMTs used in this experiment.

Repeating this measurement and Gaussian fitting with other radioactive sources, with the same $\pm 2\sigma$ BSG gate centered on the backscattered photon peak in the BSG detector, Figure 9 can be produced, allowing translation of the bar's energy axis from arbitrary ADC channel units Q_{total} to measured light produced in the bar L_{bar} in keVee. For ^{60}Co, the backscattered photons (214 keV and 210 keV) from the two emissions cannot be sufficiently distinguished from one another in the $CeBr_3$ BSG detector; however, enough difference is present in the recoil electron energies in the scintillator bar to adequately fit the projected BSG peak region with a sum of two Gaussian functions.

Energy resolution was observed to improve slightly with sources with higher-energy emissions, as expected[7] [19]. However, owing to the overall poor energy resolution, other trends related to energy resolution that were expected, such as a worsening resolution with decreasing distance between detectors, were not observed in a statistically significant manner.

While a ^{22}Na source was available, it is excluded here and demonstrates one limitation of the BSG methodology. The BSG method relies on a double coincidence between two detector elements, which corresponds to the scattering and subsequent absorption of a single photon. However, random coincidences will also satisfy the coincidence triggering logic and cause spurious events

[7] The PMT's signal amplitude is proportional to the number of photoelectrons, which is proportional to the scintillation light produced and energy deposited E. Energy resolution is defined as the ratio of the peak's FWHM to its mean, proportional to $\sqrt{E}$ and E, respectively; thus, energy resolution improves as E rises [19]. This statistical component of $\Delta E/E$ is dominant [19], though intrinsic and transfer resolutions and dark noise perturb this direct proportionality [20].

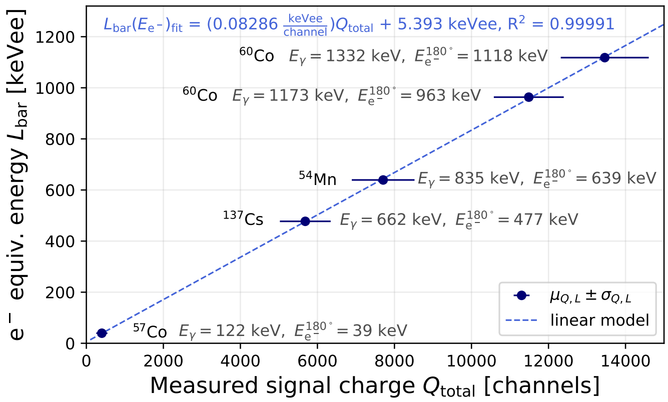

Figure 9: The calibration curve shows the linear relationship between signal charge collected Q_{total} and the electron energy deposited L for the scintillator bar. The gamma-ray emission energies and their energies imparted to electrons in 180° scatters are listed for convenience. As fit uncertainties of the means μ fall well below 1 %, the error bars instead reflect $\pm 1\sigma$ of the Gaussian peak fits. The L_{bar} axes of Figures 6 and 8 were originally in the arbitrary Q_{total} units before being converted to electron-equivalent energy with this calibration curve.

to pollute the backscattered photon data. This was found to be manageable with a source emitting two directionally-uncorrelated photons in a single decay, such as with ^{60}Co; however, the two directionally-opposite 511 keV annihilation photons of ^{22}Na result in an overwhelming abundance of unwanted triggers. While events correlated with the 511 keV emissions could be excluded with particularly high signal thresholds or energy gates, these extra complications were avoided since other sources with similar emission energies to those of ^{22}Na were already available.

The coincident time resolution is taken as the FWHM of the distribution of Δt values, differences in timestamps from the two PMTs on the ends of the long scintillator, as shown in Figure 10. Over the sixteen ^{137}Cs measurements, the time resolution also did not have a statistically significant trend dependent on p nor d and had an average value of (1.09 ± 0.06) ns for the 477 keV recoil electron peak. However, it should be noted that the 75 % CFD fraction was selected specifically to minimize the variance of the time resolution as a function of source position p and to maintain the Gaussian shape of the Δt distributions. Measurements made at 25 % CFD fraction yielded markedly skewed Δt distributions at source positions toward the bar ends and a position dependence on the time resolution, while only minimally improving the average time resolution — on the order of 50 ps.

The mean of this distribution for various source positions p along the length of the bar, shown in Figure 11, illustrates a strongly linear relationship between Δt and p. This relationship can be used to later determine interaction positions along the length of the long scintillator from the recorded Δt. The effective propagation speed of light in this scintillator/reflector combination can be inferred from double[8] the inverse of this line's slope to be 136 mm/ns, within the range of other values for EJ-200 in the literature [11, 21, 22].

[8]In obtaining the velocity, the inverse of the slope is doubled to account for the fact that the difference in the extreme values of the position p (imagining the source placed at $p = -100$ mm and $p = 100$ mm) is the full length of the bar while the difference in the extreme values of Δt is double the transit time for light to travel the full length of the bar.

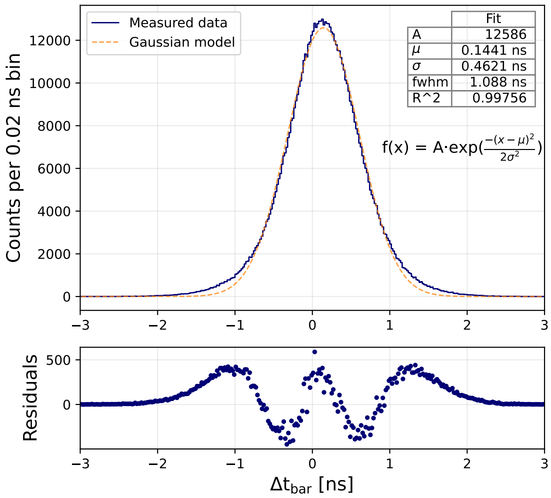

Figure 10: Δt distribution in the long scintillator bar for events falling within the BSG peak highlighted in Figure 6.

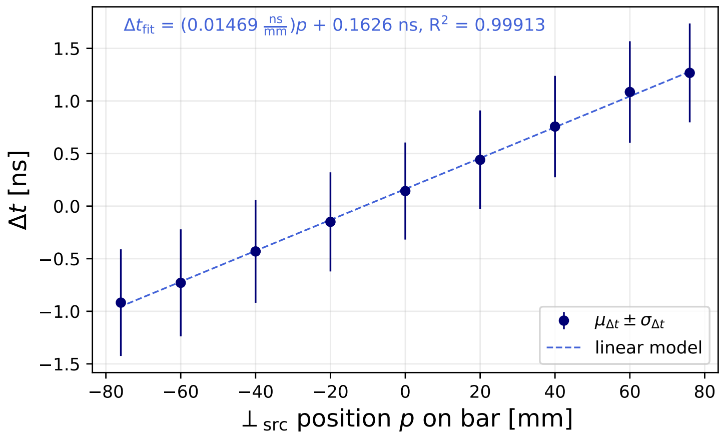

Figure 11: Mean Δt between the bar's two PMTs as a function of source location p along the bar's length. As fit uncertainties of the means μ fall well below 1 %, the error bars instead reflect $\pm 1\sigma$ of the Δt distribution Gaussian fits.

Another approach for determining interaction position involves comparing the signal strengths of the two PMTs from the scintillation light of each event. Specifically, the natural logarithm of this ratio, $\ln(Q_1/Q_2)$, is a useful and normally distributed metric, as shown in Figure 12. A strong linear relationship between source location p and the mean of the $\ln(Q_1/Q_2)$ distributions emerges, shown in Figure 13.

Furthermore, for this particular scintillator, it is clear from the relative magnitudes of the distribution widths (vertical error bars) and steepness of the slopes in Figures 11 and 13 that the interaction position is resolved with more certainty when using $\ln(Q_1/Q_2)$ instead of Δt. This relationship will vary for different scintillator and reflector materials. For instance, one may expect a less opaque (higher attenuation length) scintillator to provide higher energy resolution with

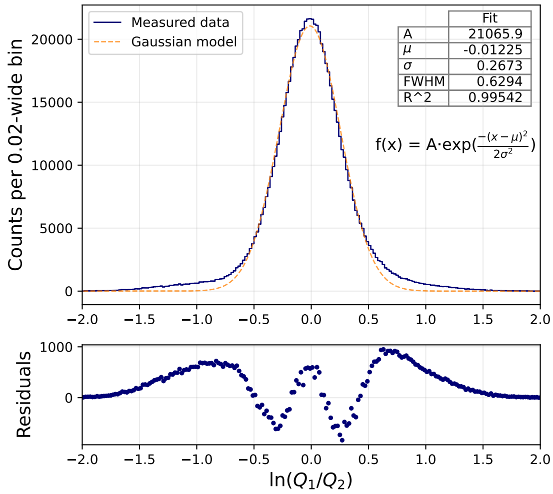

Figure 12: Distribution of the natural logarithms of the ratios of event-wise charges collected in the ends of the scintillator bar for events falling within the BSG peak highlighted in Figure 6.

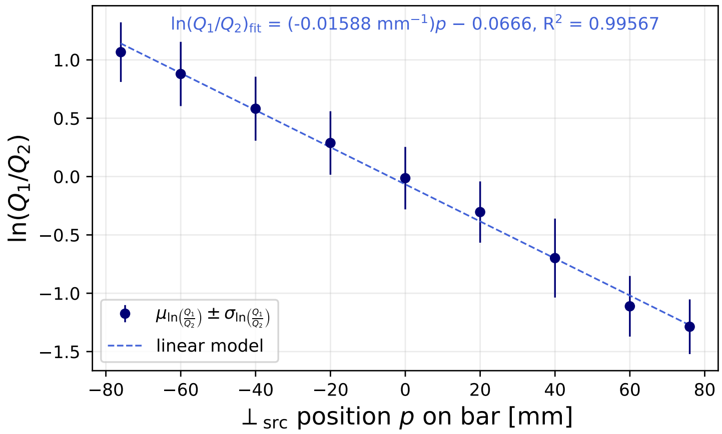

Figure 13: Mean values of the natural logarithm of the ratio of event-wise charges collected in the ends of the scintillator bar as a function of source location p along the bar's length. As fit uncertainties of the means μ fall well below 1%, the error bars instead reflect $\pm 1\sigma$ of the $\ln(Q_1/Q_2)$ distribution Gaussian fits.

superior light transmission and collection, but with less attenuation $\ln(Q_1/Q_2)$ will vary less along p, increasing difficulty in distinguishing interaction positions with confidence. For similar reasons, a scintillator with a higher effective speed of light would be expected to have more challenges discerning the position using the time differences of the two PMT signals. Choice of specular versus diffuse reflector material would also influence these properties. The position resolution is taken to be the standard deviation of the distribution of the value used to calculate position (either $\ln(Q_1/Q_2)$ or Δt), converted to units of distance in millimeters with the linear best fit equation for $\ln(Q_1/Q_2)$ (Figure 13) or Δt (Figure 11) as a function of source position p. Over the nine measurements varying lateral position p, this yields a position resolution at 477 keV of (17.1 ± 1.7) mm when using $\ln(Q_1/Q_2)$ and (32.8 ± 1.1) mm when using Δt.

An additional useful test to verify that both PMTs affixed to the bar are sufficiently optically coupled and that both halves of the bar are equal, in terms of defects and optical transport, is to compare the natural logarithm of the signal strength / light collected by each individual PMT with p, shown in Figure 14. The two fit lines intersect at the bar's center and have nearly identical, but opposite, slopes, verifying that the scintillator is of nearly uniform quality along its length and that both ends are equally sufficiently optically coupled to their PMTs.

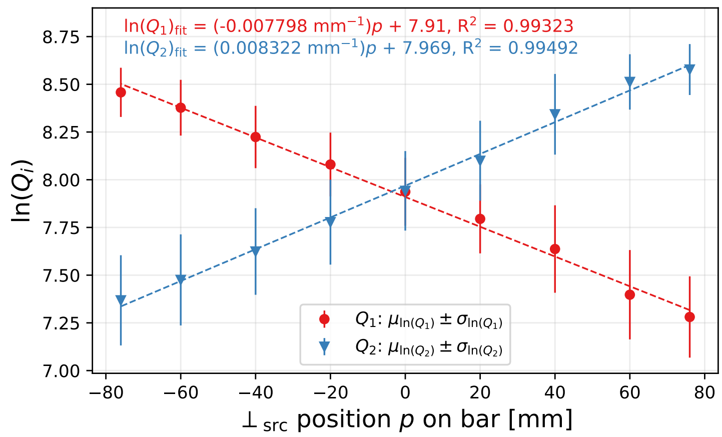

Figure 14: Natural logarithm of each bar PMT's event-wise charge collected as a function of source location p along the bar's length.

This can be quantified with the inverse of the slopes of these fit lines, yielding the technical attenuation length[9] L_{att}, which is (128 ± 4) mm and (120 ± 3) mm for Q_1 and Q_2, respectively, as described in Equation 3.2 where $d_{\text{PMT}-I_1}$ is the PMT-to-first-interaction distance, $Q_i(d_{\text{PMT}-I_1})$ is the charge signal measured in PMT i at the given distance from the interaction, Q_0 is the charge signal corresponding to 100 % of the light produced before any losses, ϵ is the optical coupling efficiency, and PDE is the PMT photon detection efficiency [24]. Taking the natural logarithm of Equation 3.2 yields Equation 3.3 (resembling the linear fit equation in Figure 14) where one can see that L_{att} and $d_{\text{PMT}-I_1}$ can be isolated from the terms to the left of the exponential, which are combined into a single term and not investigated further. The similarity in the calculated attenuation lengths for the two ends give confidence in the near uniformity of the material and optical couplings (but hint at a slight disparity between the two ends).

$$Q_i(d_{\text{PMT}-I_1}) = \frac{Q_0}{2} \cdot \epsilon \cdot \text{PDE} \cdot e^{-d_{\text{PMT}-I_1}/L_{\text{att}}} \tag{3.2}$$

$$\ln(Q_i(d_{\text{PMT}-I_1})) = \frac{-1}{L_{\text{att}}} \cdot d_{\text{PMT}-I_1} + \ln\left(\frac{Q_0}{2} \cdot \epsilon \cdot \text{PDE}\right) \tag{3.3}$$

[9]Technical attenuation length (TAL) differs from the bulk attenuation length (BAL) in that it includes effects of the geometry, surface finish, and reflective wrapping of the scintillator rather than being solely characteristic of the material/compositional properties alone [23]. The quoted attenuation length errors here are from the standard error of the determined slope of the linear regression fits.

While looking at the bar's two PMT signals individually, the portion of the time resolution attributable to the PMTs and subsequent readout electronics chain can be evaluated. Figure 15 shows the distribution of time differences between the BSG detector and PMT1/PMT2 on the scintillator bar for one of the extreme positions measured, $p = 76\,\text{mm}$. At this position, the source is much closer to PMT2 than PMT1, meaning scintillation light bound for PMT1 will undergo considerably more scattering and reflection than that bound for PMT2, and this is reflected in there being much less spread in the $\Delta t_{\text{PMT}_2-\text{BSG}}$ distribution than in the $\Delta t_{\text{PMT}_1-\text{BSG}}$ distribution.

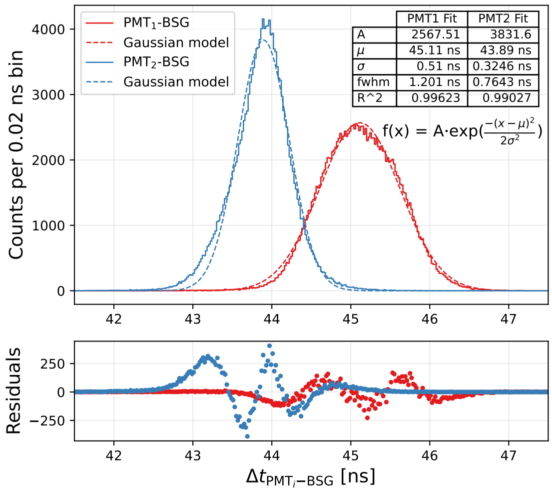

Figure 15: Δt distributions between the BSG detector and each of the PMTs affixed to the long scintillator bar for BSG peak events for ^{137}Cs at source position $p = 76\,\text{mm}$.

The FWHM of these distributions can be plotted as a function of source position p for the nine different lateral positions measured, shown in Figure 16. From the linear regression fit lines, the $\Delta t_{\text{FWHM},\text{PMT}_i-\text{BSG}}$ values can be extrapolated to the ends of the bar ($p = \pm 100\,\text{mm}$) to estimate the time resolution attributable to the PMT and the subsequent electronics chain; these are (601 ± 16) ps and (612 ± 11) ps for PMT1 and PMT2, respectively.

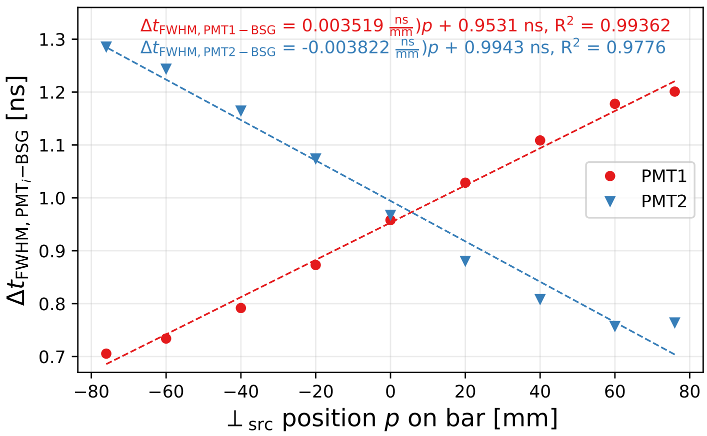

Figure 16: FWHM of the Δt distributions between the BSG detector and each of the PMTs affixed to the long scintillator bar as a function of source position p.

The nine measurements at different lateral positions p and their subsequent analyses were repeated for a detector-to-detector distance of $d = 10$ mm as well. The results obtained from this set are nearly identical to those obtained at $d = 80$ mm, well within each other's error bars, and were acquired with less time and with better counting statistics due to the substantially more favorable solid angle of the $d = 10$ mm configuration. This further emphasizes the theoretical conclusions showcased in Figure 3 that the BSG setup, when the source is affixed to the long scintillator, is quite forgiving for even rather small detector-to-detector distances, allowing for faster characterization of numerous detector elements.

Furthermore, while earlier it was noted that no trends in resolutions were statistically significant among the measurements varying detector-to-detector distance d, this is only the case for the source being affixed to the scintillator bar. An additional seven measurements were made varying d (d = 5, 10, 20, 30, 50, 80, and 150 mm) but affixing the source to the BSG detector instead. While in this additional set of measurements the expected sharpening of the energy resolution with increasing d was not observed owing to the low energy resolution — with respect to the expectations drawn from the theoretical calculations and corresponding results shown in Figure 3 — the expected worsening of the coincident time resolution with increasing d, attributable to the spatial distribution of detected BSG electrons becoming more evenly spread across the bar's length, was strongly apparent, as shown in Figure 17.

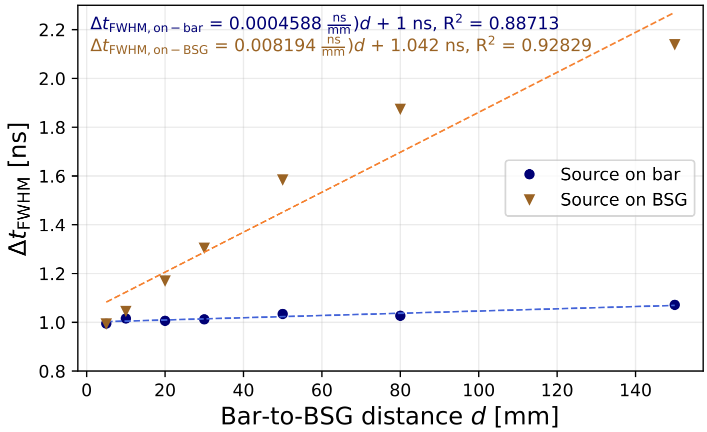

Figure 17: Time resolution Δt_{FWHM} as a function of detector-to-detector distance d for the source attached to the bar (as done throughout this work) versus attached to the BSG detector (as done traditionally when employing the BSG method [7, 10]).

4 Conclusions

The Backscatter Gating (BSG) methodology for characterization of the energy, coincident time, and position resolutions of a long form factor organic scintillator has been laid out theoretically and then demonstrated experimentally. BSG achieves this "complete" characterization (for resolutions of interest for imaging applications) in a single, relatively simple setup, reducing the experimental burden of and improving the repeatability in characterizing a large number of similar long scintillators being assembled into a larger camera-type detector arrangement. While traditional applications of BSG focused on energy resolution characterization and involved fixing the radiation source to the BSG detector face, this work demonstrated the method's applicability for time and position resolution characterization too when placing the source on the long scintillator instead. Though the low energy resolution of the scintillator and PMT combination in this work prevented discerning the expected finer trends of energy resolution with geometrical permutations, other anticipated trends were observed, and the best practices with employing the BSG methodology could be verified.

In short, when placing the radiation source onto the long scintillator and using a fairly small BSG detector, distances between the two detectors of only a few centimeters are already enough to finely confine — spatially and energetically — the events in the bar; greater distances offer diminishing returns at the expense of longer acquisition times. Smaller CFD fractions can slightly improve time resolution at the expense of time resolution uniformity along the length of the bar and its Gaussian-distributed nature, especially near the edges of the scintillator bar. Whether the readout time signal differences or the logarithms of the ratios of the readout charge signals provide superior position resolutions will depend on a number of factors specific to the scintillator composition, geometry, and assembly, and the BSG method provides a means of measuring both quantities simultaneously at a fixed energy deposition. An ideal radiation source for the BSG methodology emits a single discrete gamma ray per decay, though sources with only a few directionally-uncorrelated emissions per decay can also be used (but may require slightly higher detector-to-detector distances to minimize contamination from false coincidences, i.e., two different photons being detected simultaneously). Comparison of the slopes of the logarithms of the individual readout charge signals as a function of source position provides a means of verifying homogeneity of the scintillator bar and quality of the optical couplings and determining the technical attenuation length of the assembled scintillator.

The theory and calculations behind anticipated electron energy and position distributions for events satisfying the coincidence logic of the BSG setup are provided to allow for evaluation of the trade-offs regarding source location, detector positions, and detector geometries for an arbitrary BSG setup, not just one of similar dimensions and distances to those of this work. One important caveat is that this methodology relies on most of the recoil electrons stopping within the scintillator bar. If evaluating very thin scintillators whose widths are on the order of the recoil electron ranges or smaller, the energy deposition in the bar will cease to be constant and instead become more distributed. In such scenarios, energy resolution characterization would require a more complex measurement apparatus (for determining energies of escaping recoil electrons) and/or source (such as a fixed-energy electron beam). Conversely, with larger scintillator cross sections, this effect becomes nearly negligible. Thus, while less suitable for thin fiber-like scintillators, the BSG methodology provides a streamlined and automatable (especially if using an electric motor to shift the long scintillator — or BSG detector and source) approach for "complete" characterization of numerous long organic scintillator elements with minimal resources.

Acknowledgments

This work is supported by The Research Council of Norway grant number 301459. We would also like to thank Kristian Ytre-hauge at the University of Bergen for lending the EJ-200 scintillator and its mounted PMTs used in this work and Katja Römer at Helmholtz-Zentrum Dresden-Rossendorf for initial testing of the $CeBr_3$ BSG detector prior to its lease to the Western Norway University of Applied Sciences for the measurements conducted in this work.

References

[1] I. Meric, E. Alagoz, L.B. Hysing, T. Kögler, D. Lathouwers, W.R.B. Lionheart et al., *A hybrid multi-particle approach to range assessment-based treatment verification in particle therapy*, *Sci. Rep.* **13** (2023) 6709.

[2] M. Sweany, A. Galindo-Tellez, J. Brown, E. Brubaker, R. Dorrill, A. Druetzler et al., *Interaction position, time, and energy resolution in organic scintillator bars with dual-ended readout*, *Nucl. Instrum. Meth. A.* **927** (2019) 451.

[3] H.H. Vo, S. Kanamaru, C. Marquet, H. Nakamura, M. Nomachi, F. Piquemal et al., *Energy resolution of plastic scintillation counters for beta rays*, in *2007 IEEE Nuclear Science Symposium Conference Record*, vol. 2, pp. 1378–1385, 2007, DOI.

[4] U. Bravar, P.J. Bruillard, E.O. Flckiger, J.R. Macri, M.L. McConnell, M.R. Moser et al., *Design and Testing of a Position-Sensitive Plastic Scintillator Detector for Fast Neutron Imaging*, *IEEE Trans. Nucl. Sci.* **53** (2006) 3894.

[5] K. Roemer, G. Pausch, C.-M. Herbach, M. Kapusta, Y. Kong, R. Lentering et al., *Energy resolution and nonlinearity of NaI(Tl), CaF2(Eu), and plastic scintillators measured with the wide-angle Compton-coincidence technique*, in *IEEE Nuclear Science Symposuim & Medical Imaging Conference*, pp. 580–586, 2010, DOI.

[6] P. Limkitjaroenporrn, J. Kaewkhao, P. Limsuwan and W. Chewpraditkul, *Nonproportionality of electron response using CCT: Plastic scintillator*, *Appl. Radiat. Isot.* **68** (2010) 1780.

[7] G. Pausch, K. Roemer, C.-M. Herbach, Y. Kong, R. Lentering, C. Plettner et al., *Characterization and calibration of large-volume PVT detectors by Backscatter Gating*, in *2011 IEEE Nuclear Science Symposium Conference Record*, pp. 2214–2219, 2011, DOI.

[8] T. Baumann, J. Boike, J. Brown, M. Bullinger, J.P. Bychoswki, S. Clark et al., *Construction of a modular large-area neutron detector for the NSCL*, *Nucl. Instrum. Meth. A.* **543** (2005) 517.

[9] L. Karsch, A. Böhm, K.-T. Brinkmann, L. Demirörs and M. Pfuff, *Design and test of a large-area scintillation detector for fast neutrons*, *Nucl. Instrum. Meth. A.* **460** (2001) 362.

[10] L. Swiderski, M. Moszyński, W. Czarnacki, J. Iwanowska, A. Syntfeld-Każuch, T. Szczęśniak et al., *Measurement of Compton edge position in low-Z scintillators*, *Radiat. Meas.* **45** (2010) 605.

[11] J. Turko, R. Beyer, A.R. Junghans, I. Meric, S.E. Mueller, G. Pausch et al., *Characterization of organic glass scintillator bars and their potential for a hybrid neutron/gamma ray imaging system for proton radiotherapy range verification*, *J. Instrum.* **19** (2024) P01008.

[12] Eljen Technology, "General Purpose Plastic Scintillator: EJ-200, EJ-204, EJ-208, EJ-212 Data Sheet." Online, 2021.

[13] Hamamatsu, "Photomultiplier tubes R5611, R5611-01: For scintillation counting, ruggedized, compact, 19mm (3/4 inch) diameter, bialkali photocathode, 10–stage, head–on type." datasheet, 1995.

[14] Hamamatsu, "Photomultiplier tubes R13478, R13449, R13408, R13089, R15608." datasheet, 2020.

[15] CAEN, "DT5730 & DT5725 Digitizer User Manual." `https://www.caen.it/products/dt5730/`.

[16] CAEN, "CoMPASS Multiparametric DAQ Software for Physics Applications." https://www.caen.it/products/compass/.

[17] T. Sato, Y. Iwamoto, S. Hashimoto, T. Ogawa, T. Furuta, S.-I. Abe et al., *Recent improvements of the particle and heavy ion transport code system – PHITS version 3.33*, *J. Nucl. Sci. Technol.* **0** (2023) 1.

[18] M. Berger, J. Coursey and M. Zucker, *ESTAR, PSTAR, and ASTAR: Computer Programs for Calculating Stopping-Power and Range Tables for Electrons, Protons, and Helium Ions (version 1.21)*, 1999-01-01, 1999.

[19] G.F. Knoll, *Radiation Detection and Measurement*, Wiley (2000).

[20] P. Dorenbos, J.T.M. de Haas and C.W.E. van Eijk, *Non-proportionality in the scintillation response and the energy resolution obtainable with scintillation crystals*, *IEEE Trans. Nucl. Sci.* **42** (1995) 2190.

[21] C. Wu, Y. Heng, Y. Zhao, X. Zhao, Z. Sun, J. Wu et al., *The timing properties of a plastic time-of-flight scintillator from a beam test*, *Nucl. Instrum. Meth. A.* **555** (2005) 142.

[22] C. Betancourt, A. Blondel, R. Brundler, A. Dätwyler, Y. Favre, D. Gascon et al., *Application of large area SiPMs for the readout of a plastic scintillator based timing detector*, *J. Instrum.* **12** (2017) P11023.

[23] Łukasz Kapłon, *Technical Attenuation Length Measurement of Plastic Scintillator Strips for the Total-Body J-PET Scanner*, *IEEE Trans. Nucl. Sci.* **67** (2020) 2286.

[24] L. Cosentino, P. Finocchiaro, A. Pappalardo and F. Garibaldi, *High-resolution Time-Of-Flight PET with Depth-Of-Interaction becomes feasible: a proof of principle*, 2012. 10.48550/arXiv.1203.0043.

[25] H.N. Ratliff, *Thick-target neutron yields for intermediate-energy heavy ion experiments at NSRL*, Ph.D. thesis, The University of Tennessee, Knoxville, 2018.

A Derivation of BSG relationships

In reference to the diagram and its marked dimensions in Figure 2, this appendix derives the relationships necessary to determine the expected electron energies and expected relative intensities as a function of detector and source locations and interaction positions, illustrated earlier in Figure 3. This assumes a cylindrical BSG detector and a long rectangular-prism-shaped bar as the long scintillator. The labeled dimensions of Figure 2, along with a few useful values not illustrated, are as follows:

- $\perp_{\text{src}}$ - the line perpendicular to the long scintillator which intersects the source and BSG detector
- S - location of the radioactive source
- I_1 - location of the first photon interaction i_1, Compton scattering within the long scintillator
- I_2 - location of the second photon interaction i_2, full absorption within the BSG detector
- θ - the Compton scattering angle
- x - distance between source and long scintillator

- d - face-to-face distance between BSG detector and long scintillator
- ℓ - distance along the long scintillator of first interaction from the perpendicular $\perp_{\text{src}}$ intersecting the source and BSG detector
- w - first interaction's i_1 depth along the bar's width
- z - second interaction's i_2 depth from the BSG detector's face
- r - second interaction's i_2 radial distance from $\perp_{\text{src}}$

The distances between S, I_1, and I_2 are denoted as d_{S,I_1}, d_{I_1,I_2}, and $d_{I_2,S}$ and are:

$$d_{S,I_1} = \sqrt{(x+w)^2 + \ell^2} \tag{A.1}$$

$$d_{I_1,I_2} = \sqrt{(\ell - r)^2 + (d+w+z)^2} \tag{A.2}$$

$$d_{I_2,S} = \sqrt{r^2 + (d-x+z)^2} \tag{A.3}$$

The scattering angle θ for the Compton scatter i_1 can be found, with the aid of the law of cosines, as:

$$\begin{aligned} \theta &= \pi - \angle SI_1I_2 \\ &= \pi - \arccos\left(\frac{d_{S,I_1}^2 + d_{I_1,I_2}^2 - d_{I_2,S}^2}{2d_{S,I_1}d_{I_1,I_2}}\right) \end{aligned} \tag{A.4}$$

The recoil electron's energy E_{e^-} can then be found using the known initial photon energy E_γ and energy after the Compton scatter E'_γ (which, experimentally, is fully absorbed in the BSG detector), given the electron's rest mass energy $m_\text{e}c^2$:

$$\begin{aligned} E_{\text{e}^-} &= E_\gamma - E'_\gamma \\ &= E_\gamma\left(1 - \left(1 + \frac{E_\gamma}{m_\text{e}c^2}(1-\cos\theta)\right)^{-1}\right) \end{aligned} \tag{A.5}$$

To determine the expected detected recoil electron energy spectrum and intensities for set values of x and d, one must sample all various first interaction positions I_1 (values of ℓ) along the long scintillator's length. (This work opts for a numerical, rather than analytical, approach to this integration.) To scale the intensities of each Compton scatter interaction position, the solid angle from the source to interaction position Ω_{S,I_1}, solid angle from the first to second interaction positions Ω_{I_1,I_2}, and Klein-Nishina differential scattering cross section $d\sigma_{\text{KN}}/d\Omega$ should be accounted for. That is to say, the expected intensity Φ (relative contribution) from each position along the bar's length scales with the product of these three values.

$$\Phi \ \propto \ \Omega_{S,I_1} \cdot \Omega_{I_1,I_2} \cdot \frac{d\sigma_{\text{KN}}}{d\Omega} \tag{A.6}$$

Given the point-like nature of the source, if the length of the bar is numerically sampled in small enough slices, Ω_{S,I_1} can be proportionally approximated with just the inverse square law:

$$\Omega_{S,I_1} \propto \frac{1}{d_{S,I_1}^2} \tag{A.7}$$

With the BSG detector being a larger cylinder, its shape should be accounted for in Ω_{I_1,I_2}. This calculation uses an angle φ that is formed between the line $\perp_{\text{src}}$ and the line connecting I_1 and the center of the front face of the BSG detector. One can think of this angle φ as the angle at which I_1 "views" the BSG detector.

$$\varphi = \arctan\left(\frac{\ell}{d+w}\right) \tag{A.8}$$

The solid angle subtended by a cylinder to a point is best approximated, using its projected area $A_{\text{projected}}$ and the BSG detector's full radius R and full length Z, as [25]:

$$\begin{aligned}\Omega_{I_1,I_2} &\approx \frac{A_{\text{projected}}}{4\pi d_{I_1,I_2}^2} \\ &\approx \frac{2RZ\sin\varphi + \pi R^2\cos\varphi}{4\pi d_{I_1,I_2}^2}\end{aligned} \tag{A.9}$$

The full derivation of the projected area for a cylinder and justification of its usage in this solid angle approximation can be found in Reference 25. The Klein-Nishina differential scattering cross section $d\sigma_{\text{KN}}/d\Omega$ is purely a function of scattering angle θ and initial photon energy E_γ and is detailed in Reference 19.

Thus, the energies and intensities shown in Figure 3 are determined by slicing the length of the bar into many tiny segments and, in each, calculating the recoil electron energy E_{e^-} and its relative detection intensity Φ for a successfully detected backscatter event. The range of electron energies denoted by the bands in the plots are determined by repeating the calculation but accounting for the extreme positions of I_1 possible along the long scintillator's width and extreme positions of I_2 possible within the volume of the BSG detector instead of assuming the interactions occur along each detector's centerline.